Journal of
Materials Chemistry A

PAPER

View Article Online
View Journal | View Issue

Cite this: *J. Mater. Chem. A*, 2016, **4**, 5505

Co_3S_4@polyaniline nanotubes as high-performance anode materials for sodium ion batteries†

Qian Zhou,[a] Li Liu,*[ab] Zhifeng Huang,[a] Lingguang Yi,[a] Xianyou Wang[a]
and Guozhong Cao*[b]

In this study, by employing Co_3S_4 nanotubes prepared by a facile self-template hydrothermal route based on the Kirkendall effect, Co_3S_4@polyaniline (Co_3S_4@PANI) nanotubes, in which polyaniline is uniformly coated on both exterior and inner surfaces of Co_3S_4 nanotubes, have been fabricated through *in situ* oxidative polymerization. Benefiting from the highly conductive and mechanically robust polyaniline shell, the conductivity and stability of the composite have been significantly improved. As a result, Co_3S_4@PANI nanotubes demonstrate much better electrochemical performance than bare Co_3S_4 nanotubes as sodium ion battery anode materials, with a high capacity of 252.5 mA h g^{-1} after 100 cycles at the current density of 200 mA g^{-1}. In contrast, although a specific capacity of the bare Co_3S_4 nanotubes in the first cycle achieved was 815.3 mA h g^{-1}, it rapidly decayed to 192.9 mA h g^{-1} at the 20th cycle and further reduced to 58.2 mA h g^{-1} after 100 cycles. Furthermore, Co_3S_4@PANI nanotubes showed a high discharge capacity of 170.1 mA h g^{-1} after 400 cycles with a large current density of 4000 mA g^{-1}. The excellent electrochemical properties of Co_3S_4@PANI nanotubes were ascribed to the combination of Co_3S_4 and PANI and the stability of the composite structure.

Received 19th February 2016
Accepted 11th March 2016

DOI: 10.1039/c6ta01497f

www.rsc.org/MaterialsA

1. Introduction

The ever-growing need for high-capacity energy storage devices for applications ranging from portable electronics to electric vehicles has sparked the study of new batteries beyond Li-ion batteries.[1–3] Sodium ion batteries (NIBs) have been considered to be complementary to, or a substitute for, lithium ion batteries (LIBs). Its natural abundance, low price, similar intercalation chemistry to Li and suitable redox potential endows Na with the ability to substitute Li.[4–6] It is obvious that the ionic radius of the Na ion is larger than that of the Li ion, thus not all electrode materials suitable for LIBs are applicable for NIBs. There have been some significant advances achieved in the cathodic materials.[7–9] However, it remains a big challenge to develop suitable anode materials for NIBs.

Graphite has been widely applied in LIBs due to its large and stable capacity, but Na ion insertion into graphite is severely limited.[10,11] Although many other carbon-based materials (*e.g.*, hard carbon and carbon fibers) have been receptive towards Na^+ insertion, they rely on the presence of graphite nanocrystallites and nanovoids, which is less than ideal as the sodium insertion only takes place over a narrowly low potential range.[6,12,13] The relatively low sodium storage insertion voltage would induce the deposition of sodium metal on the surface of the anode, resulting in major safety concerns.[14]

Transition metal chalcogenides (such as SnS, MoS_2, FeS_2, and CoS_2), as a promising class of anode materials with high theoretical capacity, can store Na ions through electrochemical conversion mechanisms.[15–18] The M–S bonds in metal sulfides are weaker than the corresponding M–O bonds in metal oxides, which could be kinetically favorable for conversion reactions. Among these metal sulfides, cobalt sulfides (such as CoS, CoS_2, Co_9S_8, and Co_3S_4) have attracted increasing attention, though most research has been so far focused on their potential applications in lithium ion batteries and supercapacitors.[19–22] The electrochemistry of such materials is rich and interesting, but current literature on their applications in sodium ion batteries remains scarce. Indeed, despite the high theoretical sodium ion storage capacity of cobalt sulfides, the cycling stability and rate capability are less satisfactory, which is largely attributable to the large volume expansion/contraction during cycling and the poor electronic conductivity, and this hinders their application as anodes in NIBs. To circumvent these issues, one of the effective methods is to combine cobalt sulfide with highly conductive and stable materials such as graphene. For example, Co_3S_4 porous nanosheets embedded in graphene sheets showed a high discharge capacity of 329 mA h g^{-1} and more than 71% capacity retention was obtained after 50 cycles at 500 mA g^{-1}.[23] Recently, CoS/graphene composites were synthesized and found to possess superior sodium ion storage

---

[a] *School of Chemistry, Xiangtan University, Xiangtan 411105, Hunan, China. E-mail: liulili1203@126.com*

[b] *Department of Materials Science and Engineering, University of Washington, Seattle, WA 98195, USA. E-mail: gzcao@u.washington.edu*

† Electronic supplementary information (ESI) available. See DOI: 10.1039/c6ta01497f

properties (230 mA h g^{-1} after 100 cycles at a current density of 100 mA g^{-1}) as anode materials for NIBs.[24] However, the reported cobalt sulfide/graphene composites still exhibited less satisfactory long-term cycling stability, which perhaps originates from their poor structural stability. In addition, the fabrication process of graphene is complicated, which results in a high manufacturing cost.

Owing to its superior electrical conductivity, outstanding structural stability, and mild preparation conditions, polyaniline (PANI) has aroused much interest in LIBs.[25,26] Many electrode materials combined with PANI have been fabricated and exhibited improved electrochemical properties and battery device performance. PANI could play an important role in stabilizing the structure, decreasing the polarization between the electrode materials and the electrolyte, promoting electrolyte permeation into the surface of the active particles, and hence enhancing ionic diffusion during charge–discharge processes.[27–29] However, to the best of our knowledge, there are no reports on the introduction of PANI into cobalt sulfides for NIBs.

In the present investigation, a self-template hydrothermal route combined *in situ* oxidative polymerization method was designed and applied for the synthesis and fabrication of Co_3S_4@PANI nanotubes. Co_3S_4@PANI nanotubes demonstrated excellent electrochemical characteristics as anode materials for NIBs when compared to the bare Co_3S_4. These included long-term cycling stability, large reversible capacity, and improved rate capability. The "protective layer" formed by the polyaniline coating on both exterior and inner surfaces of the Co_3S_4 nanotubes was considered to have made an important impact on the electronic/ionic conductivities and structural stabilization.

2. Experimental

2.1. Material preparation

2.1.1. Preparation of precursors. The precursor was fabricated by a hydrothermal method.[30] In a typical synthesis, urea (0.3 g) and $CoCl_2\cdot6H_2O$ (1.2 g) were added to 50 mL of deionized water under stirring at 200 rpm for 60 min, and then it was transferred into a 100 mL Teflon-lined stainless steel autoclave, sealed and heated in an oven at 90 °C for 12 h. The pink precipitates were collected and washed with distilled water and absolute alcohol several times. Finally, the pink precipitates were dried under vacuum at 70 °C for 12 h to obtain the precursor. The precursor is $Co(CO_3)_{0.35}Cl_{0.20}(OH)_{1.10}\cdot1.74H_2O$, which has been characterized in the following discussion.

2.1.2. Synthesis of Co_3S_4 nanotubes. The precursor (0.5 g) and $Na_2S\cdot9H_2O$ (2.0 g) were added to distilled water (60 mL) under stirring at 200 rpm for 60 min. The solution was transferred into a 100 mL Teflon-lined stainless steel autoclave, sealed and heated in an oven at 160 °C for 12 h. The black precipitates were filtered, washed with deionized water and absolute ethanol several times and then were dried in vacuum at 70 °C for 20 h to obtain Co_3S_4 nanotubes.

2.1.3. Synthesis of Co_3S_4@PANI nanotubes. PVP (1.5 g, $M_W = 40\,000$) and Co_3S_4 nanotubes (0.2 g) were dispersed in 400 mL of deionized water under ultrasonication at room temperature. After 60 min, aniline (70 μL) in the presence of concentrated HCl (20 μL, 12 mol L^{-1}) was added into the solution under stirring for 12 h. In order to start the oxidative polymerization process, ammonium peroxodisulfate (APS) solution was added into the abovementioned mixture instantly under ultrasonication. The reaction lasted for 2 h at room temperature. After the reaction was complete, the product was filtered and washed with deionized water and alcohol several times. The final product was dried in a vacuum at 60 °C for 20 h to obtain the desired Co_3S_4@PANI nanotubes. The overall strategy for preparation of Co_3S_4@PANI nanotubes can be briefly described by the process depicted in Fig. 1.

For comparison, bare PANI was also prepared by similar polymerization processes without adding Co_3S_4 nanotubes.

2.2. Structure and morphology characterization

The crystal structure of the synthesized samples was determined by X-ray diffraction (XRD; Thermo Rigaku D/MAX-2500 powder diffractometer with Cu-K_α source). The morphology and microstructure of the synthesized sample were characterized by scanning electron microscopy (SEM, JEOL JSM-6610) and transmission electron microscopy (TEM, JEOL JEM-2100F with an accelerating voltage of 200 kV). Cycled cells of Co_3S_4@PANI were disassembled in the glove box, and post-cycling films were washed in polycarbonate several times and dried in vacuum overnight before TEM study. Thermogravimetric (TG) analysis was conducted on a TGA 50 instrument from 30 to 700 °C at a heating rate of 10 °C min^{-1} in air. Fourier transform infrared (FT-IR) spectra were obtained on a Nicolet 6700 spectrometer in the region 4000–400 cm^{-1}.

2.3. Electrochemical characterization

The electrodes were fabricated by mixing 70 wt% active materials, 20 wt% acetylene black, and 10 wt% polyvinylidene fluoride (PVDF) binder in *N*-methyl pyrrolidinone to form a slurry. They were then pasted on copper foil and dried under vacuum at 110 °C for 12 h. In this study, the average loading mass of active materials is 1.75 mg cm^{-2}. The half-cells were assembled with the working electrode thus fabricated, metallic sodium anode, glass fiber separator (Whatman GF/F), and 1 M $NaClO_4$ in propylene carbonate (PC) electrolyte. Assembly of the testing cells was carried out in an argon-filled glove box in which the water and oxygen concentrations were kept below 5 ppm.

All the cells were tested after ageing for 12 h. The charge–discharge cycle tests of NIBs were performed at different current densities between 0.05 and 2.0 V. Cyclic voltammetry (CV) tests and EIS experiments were performed on a Zahner Zennium electrochemical workstation at room temperature. CV tests were carried out at a scan rate of 0.1 mV s^{-1} on the potential interval 0.05–2.0 V (*vs.* Na^+/Na). The AC perturbation signal was ±5 mV and the frequency range was from 100 MHz to 100 kHz.

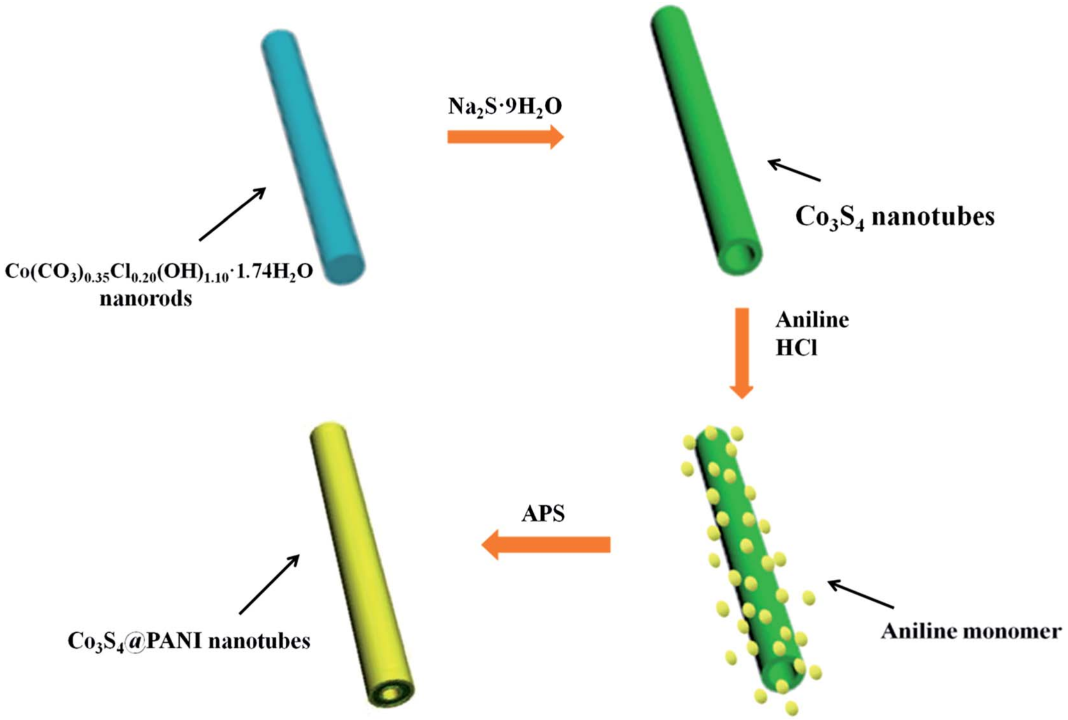

Fig. 1 Schematic for the formation of Co$_3$S$_4$@PANI nanotubes.

3. Results and discussion

3.1. Structure characterization of the intermediate precursor material

Fig. 2a shows the XRD pattern of the intermediate precursor material, which can be indexed to the crystalline Co(CO$_3$)$_{0.35}$Cl$_{0.20}$(OH)$_{1.10}$·1.74H$_2$O lattice (PDF no. 38-547). However, there are two peaks at 44.1° and 68.4°, which can be assigned to CoCO$_3$ (PDF no. 11-0692). It should also be noted that the peak intensities do not agree well with the standard card, suggesting there is a strong crystal orientation preference, though it was not possible to determine the preferential orientation in the current study. The FT-IR spectrum of the precursor, Co(CO$_3$)$_{0.35}$Cl$_{0.20}$(OH)$_{1.10}$·1.74H$_2$O, is shown in Fig. 2b. There is a broad band at 3540 cm^{-1} attributed to the O–H vibration of a hydrogen-bonded water molecule. In addition to the δH$_2$O vibration at 1637 cm^{-1}, there are some bands located below 1500 cm^{-1}, which are ascribed to Co–OH and CO$_3{}^{2-}$ bonds.[31,32] Fig. 2c shows the typical scanning electron microscopy (SEM) image of the precursor, Co(CO$_3$)$_{0.35}$Cl$_{0.20}$(OH)$_{1.10}$·1.74H$_2$O, from which a large number of rod-shaped crystals of 100–200 nm in diameter and several micrometers in length can be observed. Fig. 2d shows the transmission electron microscopy (TEM) image for the precursor, Co(CO$_3$)$_{0.35}$Cl$_{0.20}$(OH)$_{1.10}$·1.74H$_2$O, showing the solid nanorods with smooth surfaces. The selected area electron diffraction (SAED) pattern (the inset in Fig. 2d) exhibits sharp diffraction spots, indicating the single crystal nature and the good crystallinity of the Co(CO$_3$)$_{0.35}$Cl$_{0.20}$(OH)$_{1.10}$·1.74H$_2$O nanorods obtained, which corroborates with the altered XRD peak intensity and the smooth surface of the nanorods revealed by SEM and TEM images.

3.2. Structure characterization of the Co$_3$S$_4$ and Co$_3$S$_4$@PANI nanotubes

The crystallographic structures of Co$_3$S$_4$ and Co$_3$S$_4$@PANI were characterized by X-ray powder diffraction (Fig. 3a). All the diffraction peaks in both Co$_3$S$_4$ and Co$_3$S$_4$@PANI samples can be attributed and indexed to the standard XRD pattern of Co$_3$S$_4$ (PDF no. 47-1738) with a normal spinel structure (space group *Fd*3*m*). No secondary or parasitic phases of cobalt sulfides, such as CoS, CoS$_2$ and Co$_9$S$_8$, are detected, indicative of the phase purity of Co$_3$S$_4$ in the products. Although the Co$_3$S$_4$@PANI sample is coated by PANI, no change was found in the XRD pattern, as PANI is amorphous. To confirm the existence of PANI, FT-IR tests were performed and the spectra are shown in Fig. 3b. The peaks at about 3450 cm^{-1} observed in the spectra of bare PANI, bare Co$_3$S$_4$ and Co$_3$S$_4$@PANI composite can be attributed to the –OH groups of adsorbed water molecules. The bands in the range 1200–1400 cm^{-1} of bare PANI are the C–N stretching bands of an aromatic amine and the band at 1153 cm^{-1} is the N=Q=N stretching band is a characteristic of polyaniline base.[33,34] A strong peak at 1128 cm^{-1} is attributed to the Co=S stretching mode in Co$_3$S$_4$.[35] The FT-IR spectrum of Co$_3$S$_4$@PANI nanotubes is different from that of bare Co$_3$S$_4$. It can be observed from the FT-IR spectrum of Co$_3$S$_4$@PANI that the characteristic absorption band of Co$_3$S$_4$ (1128 cm^{-1}) is overlapped by the bands of PANI at 1154 cm^{-1}. It is obvious that Co$_3$S$_4$@PANI composite shows characteristic absorption bands of PANI at about 1473, 1317 and 1154 cm^{-1}, indicating the existence of PANI in the Co$_3$S$_4$@PANI nanotubes composite. TG analysis was carried out in air at a heating rate of 10 °C min^{-1} to estimate the amount of PANI in the Co$_3$S$_4$@PANI composite.

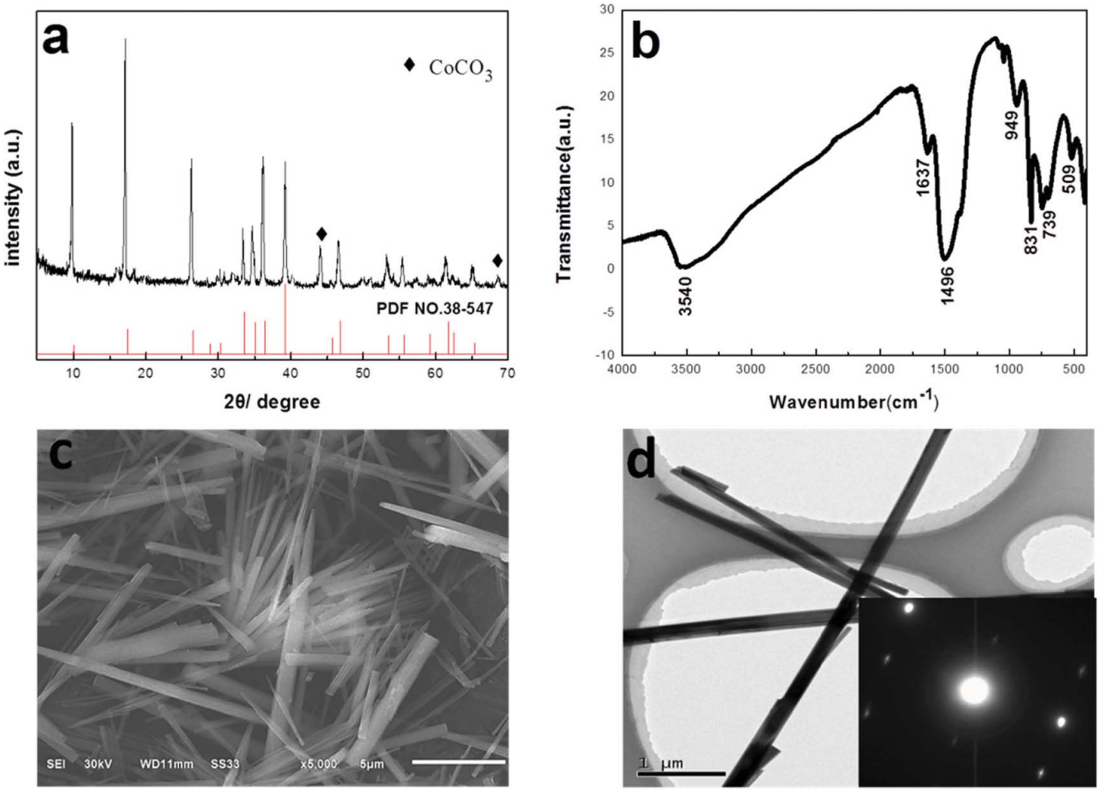

Fig. 2 (a) XRD patterns, (b) FT-IR spectrum, (c) SEM image and (d) TEM image (the inset is the SEAD pattern) of $Co(CO_3)_{0.35}Cl_{0.20}(OH)_{1.10}\cdot1.74H_2O$ nanorods.

Fig. 3c compares the TG curves of Co_3S_4@PANI and bare Co_3S_4 and shows several stages of weight loss, which could be ascribed to different phase changes in air. The weight losses up to 700 °C for bare Co_3S_4 and Co_3S_4@PANI composite are 7.2 wt% and 28.4 wt%, respectively. For bare Co_3S_4, the main weight loss stage is between 25 and 100 °C, which corresponds to the removal of moisture in the sample. For Co_3S_4@PANI composite, there is a huge weight loss from 440 °C to 580 °C, which can be mainly attributed to the decomposition and oxidative combustion of polyaniline.[36] From the TG analyses of both Co_3S_4@PANI composite and bare Co_3S_4, the content of PANI in the Co_3S_4@PANI composite is estimated to be approximately 21.2 wt%, which is lower than the content of 26.3 wt% added to the system during the synthesis. The difference between actual and theoretical content can be ascribed to the incomplete polymerization of aniline.

Fig. 4 shows the typical SEM images showing the morphology and particle sizes of Co_3S_4 and Co_3S_4@PANI composites. Fig. 4a and b reveal that Co_3S_4 nanotubes are open ended, indicating a hollow morphology. The dimensions of Co_3S_4 nanotubes are about 100–500 nm in diameter and several micrometers in length. The formation mechanism of the Co_3S_4 nanotubes can be explained based on the Kirkendall effect of the sacrificial template of $Co(CO_3)_{0.35}Cl_{0.20}(OH)_{1.10}\cdot1.74H_2O$ nanorods. The Kirkendall effect, first reported in 1942, involves unequal diffusion at an interface of two growth species with different diffusion rates.[37] The faster diffusing component will quickly diffuse out toward the interface where the formation reaction takes place and the new phase forms, resulting in inward diffusion of vacancies, which agglomerate into voids or are annihilated at dislocations or grain boundaries. In the present study, it is hypothesized that Co ions possess fast diffusion, resulting in a depletion of $Co(CO_3)_{0.35}Cl_{0.20}(OH)_{1.10}\cdot1.74H_2O$ nanorods, while S^{2-} ions generated from Na_2S have slow diffusion and react with the $Co(CO_3)_{0.35}Cl_{0.20}(OH)_{1.10}\cdot1.74H_2O$ nanorods on the surface to produce Co_3S_4 nanocrystallites. As the outward transport rate of cobalt ions through the formed cobalt sulfide shell is much faster than the inward transport rate of S^{2-} species, the cobalt sulfide shell will grow outward with an increasing diameter and the $Co(CO_3)_{0.35}Cl_{0.20}(OH)_{1.10}\cdot1.74H_2O$ core will be depleted gradually and eventually disappear to create the hollow space inside,[38,39] forming the tubular structure. Fig. 4c and d give the representative SEM images of Co_3S_4@PANI composite. After applying a PANI coating, the morphology of the Co_3S_4 nanotubes was retained, but the surface of the Co_3S_4@PANI nanotubes become rougher than the surface of bare Co_3S_4 nanotubes, suggesting that the Co_3S_4 nanotubes have been wrapped with a PANI layer. It is noted that the Co_3S_4@PANI nanotubes are connected to each other by flocculent PANI to form a more robust bundle structure, as shown in Fig. 4c.

Fig. 5a shows a TEM image of the Co_3S_4 nanotubes. The clear contrast between the dark edge and the gray center of each

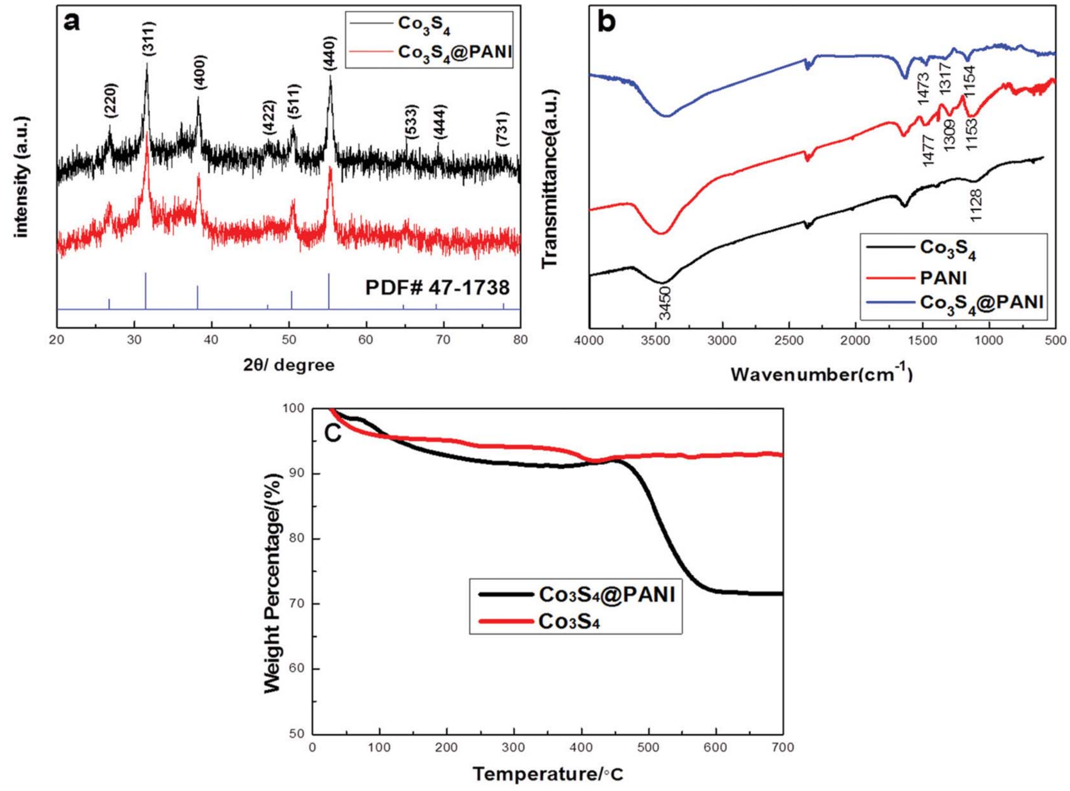

Fig. 3 (a) XRD patterns of Co_3S_4 and Co_3S_4@PANI composite. (b) FT-IR spectra of Co_3S_4, PANI and Co_3S_4@PANI composite. (c) TGA curves of the Co_3S_4 and Co_3S_4@PANI composite.

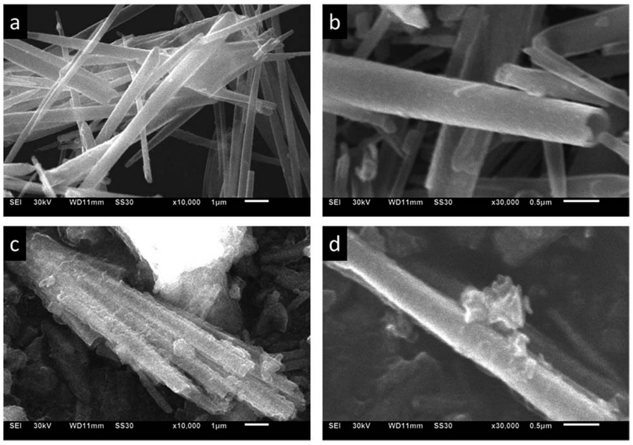

Fig. 4 (a) and (b) SEM images of Co_3S_4 nanotubes; (c) and (d) SEM images of Co_3S_4@PANI nanotubes.

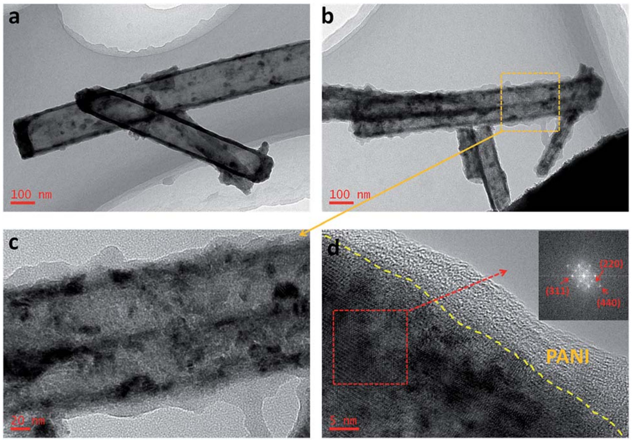

Fig. 5 (a) TEM image of Co_3S_4 nanotubes; (b) and (c) TEM and (d) HRTEM images of Co_3S_4@PANI nanotubes. The inset of (d) shows the corresponding FFT pattern of Co_3S_4@PANI nanotubes.

nanotube reveals the hollow morphology, which is in agreement with the SEM observations. The TEM image (Fig. 5b) shows that Co_3S_4 nanotubes are not only coated very well by flocculent PANI, but that they are also linked to other nanotubes by PANI coating. Owing to the hollow Co_3S_4 nanotubes' structure with open ends, the aniline molecules can penetrate and deposit on the inner walls of the nanotubes, so the inner surface of the Co_3S_4 nanotubes is also coated by a PANI layer. The flexible PANI layer coated on both exterior and inner surfaces of Co_3S_4 nanotubes would form "protective layers", thus preventing the structure from collapse during cycling. In addition, the PANI coatings contribute to the formation of conductive networks and connect individual nanotubes, therefore the electrons can be readily transmitted to the sites where redox reactions take place. Representative high resolution TEM (HRTEM) images taken near the edge of a PANI coated Co_3S_4 nanotube are shown in Fig. 5c and d. The PANI layer is typically 5–8 nm in thickness, though the PANI layer can be 20 nm thick in some regions. An HRTEM image taken of the Co_3S_4@PANI composite shows that Co_3S_4 displays clear crystal lattices, its fast Fourier transform (FFT) image of the same region (see the inset of Fig. 5d) reveals the diffraction spots have a lattice spacing related to the (311), (220) and (440) planes, which agree well with the XRD results shown in Fig. 3a.

3.3. Electrochemical properties

The cyclic voltammograms (CV) of the Co_3S_4 and Co_3S_4@PANI composite at a scan rate of 0.1 mV s^{-1} in the potential window from 0.05 to 2.0 V (*versus* Na/Na^+) are shown in Fig. 6a and b. From Fig. 6a, the cathodic peak at 0.98 V in the first scan is commonly assigned to an initial process of Na^+ insertion reaction:[23,40]

$$Co_3S_4 + xNa^+ + xe^- \rightarrow Na_xCo_3S_4 \quad (1)$$

A sharp peak at 0.72 V is related to the conversion reaction of Co_3S_4 with Na and the formation of solid electrolyte interphase:

$$Na_xCo_3S_4 + (8 - x)Na^+ + (8 - x)e^- \rightarrow 4Na_2S + 3Co \quad (2)$$

The theoretical specific discharge capacity of Co_3S_4 is 702.8 mA h g^{-1}, which is calculated based on the transfer of $8e^-$ per mole.[41] It is noted that the initial specific capacity of bare Co_3S_4 is larger than the theoretical specific capacity, probably attributable to the formation of solid electrolyte interphase (SEI). For the anodic process, the strong oxidation peak at 1.77 V can be assigned to the reverse conversion reaction of Co with Na_2S:[23,40]

$$3Co + 4Na_2S \rightarrow 8Na + Co_3S_4 \quad (3)$$

The peaks in the first scan are different from the subsequent scans in both voltage and current intensity. In the second and third scans, the cathodic peak at 0.98 V is shifted to 1.28 V and the peak at 0.72 V is divided into two peaks at 0.92 V and 0.54 V, which correspond to the process of Na^+ insertion reaction and the conversion reaction of Co_3S_4 with Na. The reduction peak of 0.72 V is divided into two peaks, whereas the oxidation peaks show little change in the first three cycles as the initial Na^+ insertion into Co_3S_4 is very slow and requires an overvoltage.[42] The CV curves of Co_3S_4@PANI composite (Fig. 6b) are similar to that of pristine Co_3S_4. The second cycle CV curve of Co_3S_4@PANI composite is largely overlapped with that of the third cycle, but there is a substantial decrease in the peak intensity for bare Co_3S_4 which indicates that the sodium insertion and extraction reactions in Co_3S_4@PANI composite are more

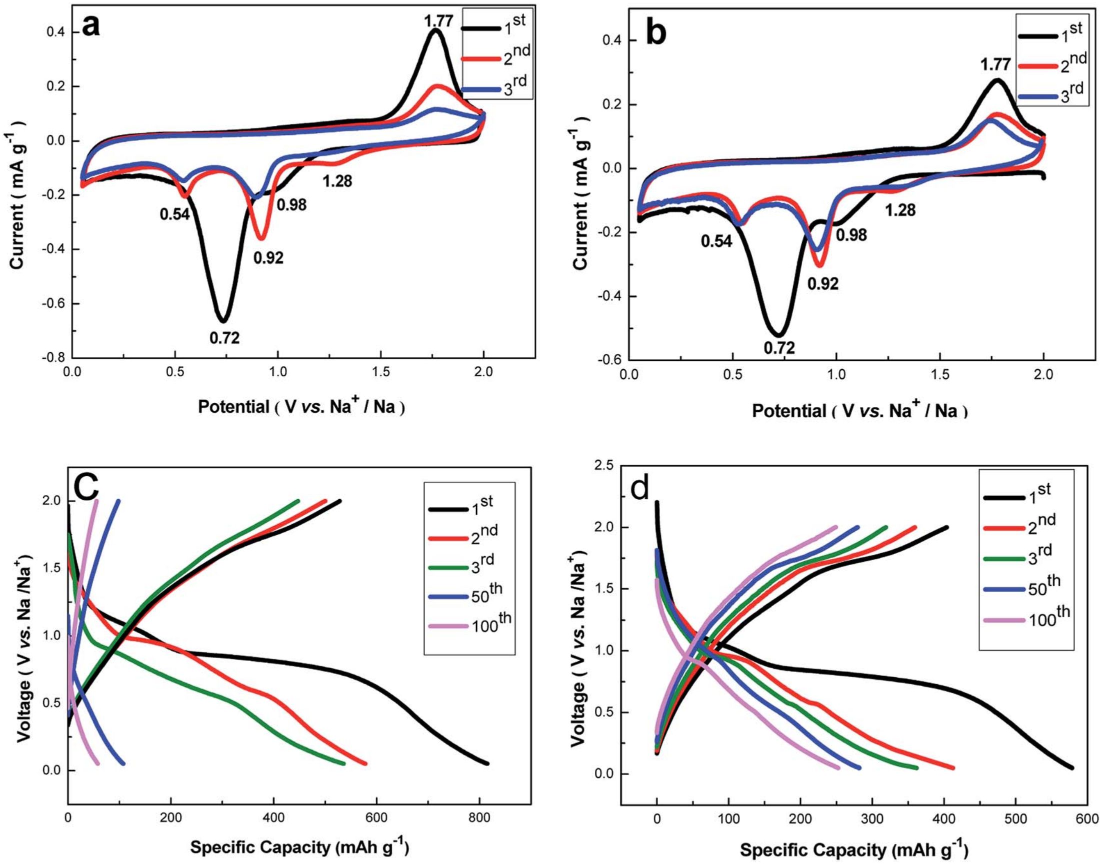

Fig. 6 Representative cyclic voltammograms (CVs) at a scan rate of 0.1 mV s^{-1}: (a) bare Co_3S_4 and (b) Co_3S_4@PANI composite. Charge–discharge profiles at a current density of 200 mA g^{-1}: (c) bare Co_3S_4 and (d) Co_3S_4@PANI composite.

reversible compared to those in bare Co_3S_4. Fig. 6c and d compare the charge–discharge voltage profiles of Co_3S_4 and Co_3S_4@PANI composite in the 1st, 2nd, 3rd, 50th and 100th cycles at a current density of 200 mA g^{-1} in the voltage window of 0.05–2.0 V. The two samples show sloped reaction plateaus located at 0.98 V and 0.72 V during the discharging process and at 1.77 V in the charging process during the first cycle, then the discharge plateaus are located at 1.28 V, 0.92 V and 0.54 V in the second and third cycles, which is in good accord with the CV curves. The discharge and charge capacities for Co_3S_4@PANI composite in the first cycle are 578.8 and 403.6 mA h g^{-1}, respectively, with a coulombic efficiency of 70%. In contrast, the first discharge and charge capacities of bare Co_3S_4 are 815.3 and 528.7 mA h g^{-1}, respectively, corresponding to a coulombic efficiency (65%), lower than that of the Co_3S_4@PANI composite. The initial capacity loss may result from the formation of the SEI and the irreversible conversion reaction between Na and Co_3S_4.[41] It is obvious that the capacity of Co_3S_4@PANI does not have a huge decay from the 3rd cycle to the 100th cycle. However, the charge–discharge voltage plateau of Co_3S_4 in the 50th cycle can hardly be observed and it experiences an obvious decrease for bare Co_3S_4 from the 3rd cycle to the 100th cycle. As observed from the voltage profiles, Co_3S_4@PANI composite shows enhanced electrochemical capacity when compared with bare Co_3S_4.

As shown in Fig. 7a, the cycling performances of bare Co_3S_4, PANI, Co_3S_4@PANI composite were tested at the current density of 200 mA g^{-1} over the range of 0.05–2.0 V. The corresponding coulombic efficiencies are also presented in Fig. 7a. Co_3S_4 nanotubes show an outstanding initial discharge capacity of 815.3 mA h g^{-1} due to their unique 1D nanotubes with open ends allowing the electrolyte to penetrate and access both inner and outer surfaces, bringing a large electrode–electrolyte contact area, rich accessible electro-active sites, and a fast Na^+ diffusion path. However, a rapid decay of capacity is observed in bare Co_3S_4 during the first few cycles and the capacity shows a continuous decrease to 192.9 mA h g^{-1} with a huge capacity loss of 76.3% after merely 20 cycles, dropping further to a low discharge capacity (58.2 mA h g^{-1}) after 100 cycles. The structure deformation of Co_3S_4 during cycling is the main factor responsible for huge capacity fading in the first 20 cycles.[43] The bare Co_3S_4 nanotubes may degrade or even pulverize during long-term cycling because the hollow structure without protection would expand during sodiation and shrink during desodiation. Co_3S_4@PANI nanotubes showed a much lower initial specific capacity than bare Co_3S_4 nanotubes, which is mainly due to the low specific capacity of PANI and the lower specific surface area. It can be seen from Fig. S1† that the specific surface area of Co_3S_4@PANI composite (8.8 m^2 g^{-1}) is lower than that of bare Co_3S_4 (19.7 m^2 g^{-1}). Although the capacity of Co_3S_4@PANI nanotubes decreases rapidly in the first and second cycles, it turns out to be stable from the 3rd cycle to the 100th cycle. The Co_3S_4@PANI composite delivers a discharge capacity of 578.8 mA h g^{-1} in the first cycle, and the capacity

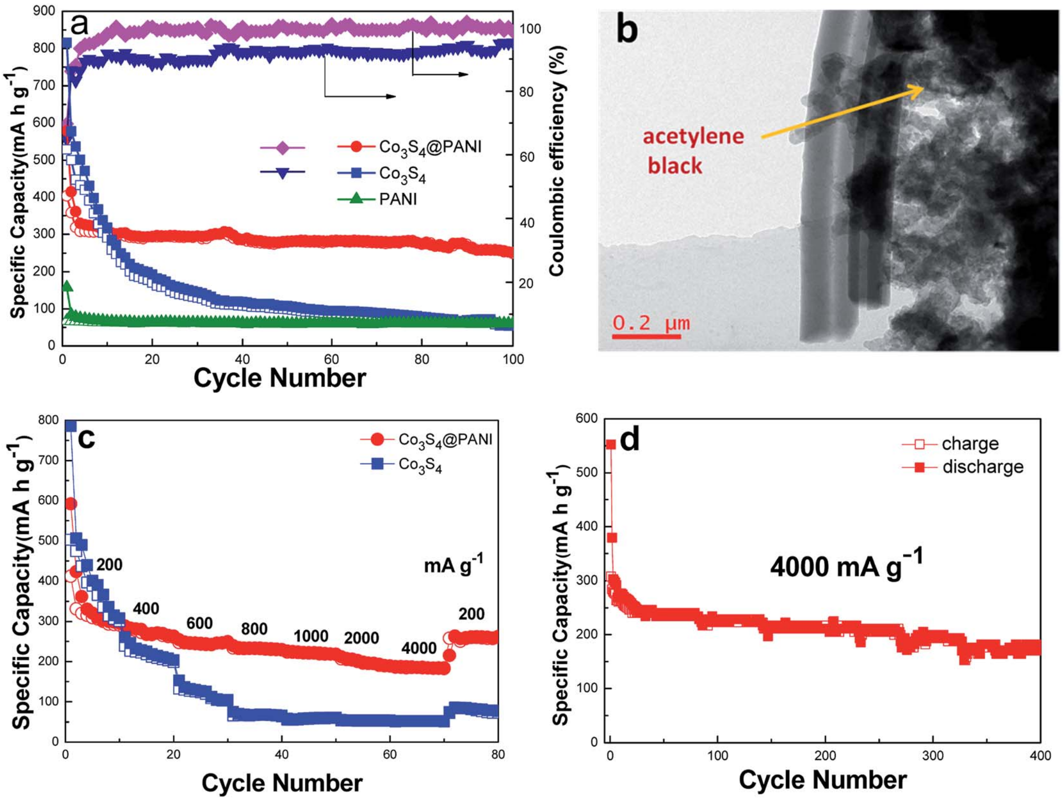

Fig. 7 (a) Cycling performance of Co_3S_4, PANI, Co_3S_4@PANI electrodes at 200 mA g^{-1} for 100 cycles. (b) TEM images of the Co_3S_4@PANI electrodes after 100 cycles of the charge–discharge process. (c) Rate performance of Co_3S_4 and Co_3S_4@PANI electrodes. (d) Long cycling performance of Co_3S_4@PANI electrodes at 4000 mA g^{-1} for 400 cycles (solid: discharge; hollow: charge).

remains at 252.5 mA h g^{-1} after 100 cycles, which is nearly five times that of the Co_3S_4 sample. In addition, the coulombic efficiencies for Co_3S_4@PANI composite are considerably higher than those of bare Co_3S_4 from the 1st to 100th cycles. For bare PANI, the specific discharge capacity is 157.4 mA h g^{-1} in the first cycle and it drops dramatically by half, in the second cycle to about 84.2 mA h g^{-1}. Bare PANI delivers an excellent capacity retention capability with almost no capacity fading from the 2nd cycle to the 100th cycle. Despite the influence of PANI in the initial few cycles, the cycle stability is greatly improved. It is noteworthy that the soft PANI coatings on the outer and inner surfaces of Co_3S_4 nanotubes would form "protective layers", which can effectively protect active materials from pulverization and avoiding structure collapse during the discharge–charge process. The Co_3S_4 nanotubes are also connected by the PANI coating, thus further improving the stability of the structure. The combination of Co_3S_4 nanotubes and PANI contributes to the improved electrochemical properties. To further attest the structural stability of the Co_3S_4@PANI composite, TEM study of Co_3S_4@PANI composite after 100 discharge–charge cycles was performed (see Fig. 7b). It is revealed that the walls of Co_3S_4@PANI nanotubes are much thicker after 100 discharge–charge cycles than those of fresh Co_3S_4@PANI nanotubes, which can be explained by the large volume expansion during cycling. However, the morphology of the Co_3S_4@PANI nanotubes remains intact after 100 cycles, indicating the excellent structural robustness of Co_3S_4@PANI nanotubes. Due to the PANI coating on both inner and outer surfaces of the Co_3S_4 nanotubes, structure collapse and pulverization caused by volume expansion were effectively suppressed.

Fig. 7c shows the rate capability of bare Co_3S_4 and Co_3S_4@PANI composite from 200 to 4000 mA g^{-1}. For each current density, the measurements were taken for 10 cycles. The discharge capacity of bare Co_3S_4 is 307.6 mA h g^{-1} at a current density of 200 mA g^{-1} after 10 cycles; however, the specific discharge capacity is 203.6 and 51.3 mA h g^{-1} at the current density of 400 and 4000 mA g^{-1}, respectively. After the high current density of 4000 mA g^{-1}, the specific discharge capacity of 75.9 mA h g^{-1} remained when the current density was reduced to 200 mA g^{-1}. As expected, the Co_3S_4@PANI electrode shows superior rate performance. When increasing the cycling current density, the Co_3S_4@PANI composite exhibits decent capacity retention: 295.5 mA h g^{-1} (200 mA g^{-1}), 218.6 mA h g^{-1} (1000 mA g^{-1}), 189.3 mA h g^{-1} (2000 mA g^{-1}). Even after a 20-fold increase in the current density to 4000 mA g^{-1}, a high discharge capacity of 184.1 mA h g^{-1} could still be retained. When reducing the current density to 200 mA g^{-1}, the specific discharge capacity of 262.3 mA h g^{-1} finally remained, which is much higher than that of the bare Co_3S_4 electrode (75.9 mA h g^{-1}). The results suggest that the introduction of PANI coating offers a 3D conductive network connecting the individual nanotubes whereby the electrons can be readily transmitted to the sites where redox reactions take place thus leading to superior rate capability. The cycling performance of Co_3S_4@PANI composite at a high current density of 4000 mA g^{-1} has been examined for 400 cycles and the results are presented in Fig. 7d. Co_3S_4@PANI composite retained a high discharge capacity of about 170.1 mA h g^{-1} after 400 cycles.

Table 1 compares the previous results reported for PANI-based and cobalt sulfide-based electrode materials for sodium ion batteries with the results of our study. As can be seen, sulfonated polyaniline shows good capacity retention, but the capacity is too low to be used as anode materials for sodium ion batteries,[44] and even polystyrene/polyaniline/graphene hybrid materials also show a low capacity of 155 mA h g^{-1} in the range of 0.02–3.0 V at 100 mA g^{-1}.[45] The bare SnO_2 particle anode shows quick capacity fading and can only deliver a considerably lower capacity of 14.4 mA h g^{-1} after 400 cycles, but PANI coating can improve the cyclability of SnO_2 remarkably. A SnO_2 hollow spheres–polyaniline composite delivers a relatively high reversible capacity of 213.5 mA h g^{-1} after 400 cycles at 300 mA g^{-1} in the range of 0.01–2.0 V.[46] Cobalt sulfides have high theoretical specific capacity but their cycle performance is very poor; graphene could obviously enhance their cyclability.[23,24,47] CoS@rGO delivers a discharge capacity of 230.8 mA h g^{-1} after 100 cycles at 100 mA g^{-1} in the range of 0.05–2.0 V.[24] When increasing the upper cut-off voltage to 2.9 V, CoS@rGO has an initial discharge capacity of 620 mA h g^{-1} at 1000 mA g^{-1} in the range of 0.1–2.9 V, and the capacity remains at 148.3 mA h g^{-1} after 500 cycles.[47] It is interesting that when increasing the lower cut-off voltage to 0.6 V, CoS@rGO shows outstanding specific capacity and cycle performance in the range of 0.6–2.9 V.[47] However, it should be noted that for anode materials, the specific capacity above 2.0 V is not so meaningful and the

Table 1 Comparison of electrochemical properties of PANI-based and cobalt sulfide-based electrode materials for sodium ion batteries

Synthesis method	Samples	Voltage range (V)	Current density (mA g^{-1})	Capacity (mA h g^{-1}) (cycle number)
Chemical oxidative copolymerization[44]	PANS	1.8–3.7	100	123 (3)–118 (200)
In situ reduction of graphene and self-assembly[45]	PS-PANI/rGO	0.02–3.0	100	852 (1)–155 (150)
Hydrothermal method and *in situ* chemical polymerization[46]	SnO_2@PANI	0.01–2.0	300	667.8 (1)–213.5 (400)
Hydrothermal method[24]	CoS@rGO	0.05–2.0	100	567.3 (1)–230.8 (100)
Solvothermal method[47]	CoS@rGO	0.1–2.9	1000	620 (1)–148.3 (500)
		0.6–2.9	1000	581 (1)–420 (1000)
Hydrothermal method[23]	Co_3S_4-PNS/GS	0.05–3.0	500	900 (1)–329 (50)
Present work: hydrothermal method and *in situ* oxidative polymerization	Co_3S_4@PANI	0.05–2.0	4000	550 (1)–170.1 (400)
		0.05–2.0	200	578.8 (1)–252.5 (100)

electrochemical properties at lower voltage range (below 0.6 V) are more important. Co_3S_4 porous nanosheets embedded in graphene sheets (Co_3S_4-PNS/GS composites) show a relatively high capacity of 329 mA h g^{-1} after 50 cycles at 500 mA g^{-1} at a cut-off voltage up to 3.0 V.[23] However, electrochemical properties from only 50 cycles are shown in this study. In a narrow voltage range (0.05–2.0 V), the Co_3S_4@PANI in this study delivers a specific capacity of 252.5 mA h g^{-1} after 100 cycles at 200 mA g^{-1}, which is larger than those of PANS,[44] PS-PANI/rGO,[45] and CoS@rGO prepared by the hydrothermal method.[24] In addition, Co_3S_4@PANI shows an excellent cycle performance, delivering 170.1 mA h g^{-1} after 400 cycles at a very high current rate of 4000 mA g^{-1}. Obviously, the electrochemical cyclability of Co_3S_4@PANI is comparable to the CoS@rGO prepared by the solvothermal method[47] and much better than the Co_3S_4-PNS/GS composites.[23]

The three-dimensional Nyquist plots of Co_3S_4 and Co_3S_4@-PANI electrodes after cycling for different numbers of cycles at around 1.28 V are shown in Fig. 8. Nyquist plots are fitted with the equivalent circuit model (Fig. 8c) and agree well with the experimental data listed in Table 2. R_e stands for the internal resistance of the test batteries, R_f is related to contact resistance and R_{ct} is the charge-transfer resistance. It is clear from Table 2 that the R_e values of both Co_3S_4 and Co_3S_4@PANI electrodes after different cycling are almost the same throughout the experiments because of the same electrolyte and fabrication parameters. The growth of R_f in bare Co_3S_4 and Co_3S_4@PANI electrodes is caused possibly by the change of morphology of

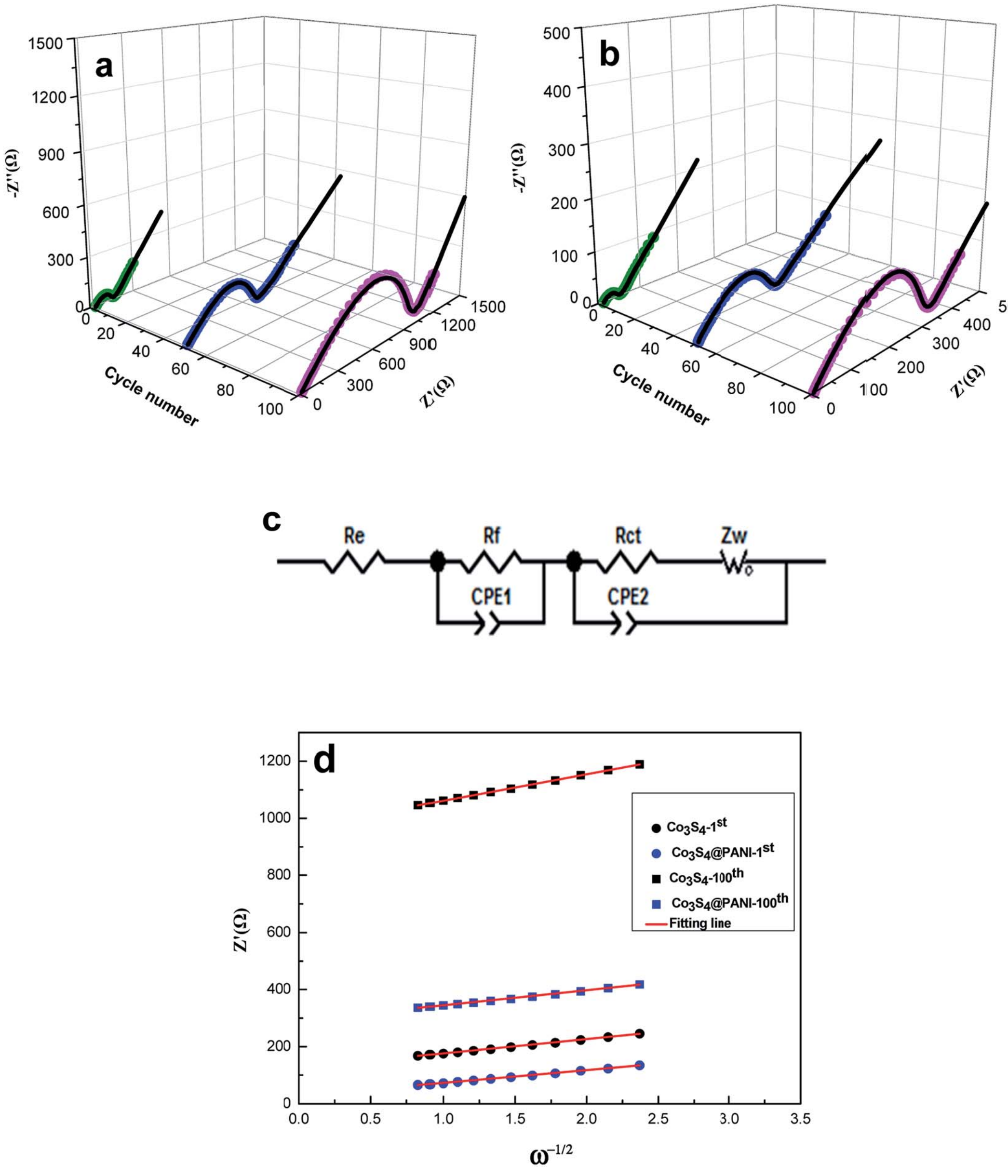

Fig. 8 Three-dimensional Nyquist plots measured for (a) Co_3S_4 and (b) Co_3S_4@PANI composite around 1.28 V after different numbers of cycles at 200 mA g^{-1} in Na half-cells; (c) the equivalent circuit model; (d) the relationship plot between Z_{re} and $\omega^{-1/2}$ in the low-frequency region.

Table 2 R_e, R_f and R_{ct} values of Co_3S_4 and Co_3S_4@PANI composite after different cycles in Na half-cells derived from the EIS results

	R_e			R_f			R_{ct}		
Samples	1st	50th	100th	1st	50th	100th	1st	50th	100th
Co_3S_4	8.6	9.2	10.7	11.5	63.7	92.7	102.4	503.1	894.3
Co_3S_4@PANI	8.3	8.8	9.1	10.2	32.6	48.5	27.8	169.0	259.8

the particles. The R_{ct} of the Co_3S_4 sample is 102.4 Ω after 1 cycle and this value increases to 894.3 Ω after 100 cycles, which is consistent with the trend of huge capacity loss during the 100 cycles. It is well known that the growth of R_{ct} means the increase of polarization. However, the R_{ct} of the Co_3S_4@PANI sample is 27.8 Ω after 1 cycle, whereas this value only increases to 259.8 Ω after 100 cycles. It is obvious that the R_{ct} of Co_3S_4@PANI is much lower than that of bare Co_3S_4, indicating the great decrease of charge-transfer resistance at the electrode–electrolyte interface owing to combination with the conductive PANI. The sodium ion diffusion coefficient can be calculated according to the following equation:[48]

$$D = \frac{R^2T^2}{2A^2n^4F^4c^2\sigma_w{}^2} \tag{4}$$

where R is the gas constant, T is the absolute temperature, A is the surface area of the cathode, n is the number of electrons per molecule during oxidization, F is the Faraday constant, c is the concentration of sodium ions, and σ_w is the Warburg factor related to Z':

$$Z' = R_e + R_f + R_{ct} + \sigma_w\omega^{-1/2} \tag{5}$$

where ω is the angular frequency in the low frequency region. The relationship plot between Z_{re} and reciprocal square root of the angular frequency ($\omega^{-1/2}$) in the low-frequency region is shown in Fig. 8d. The sodium ion diffusion coefficients (D_{Na}) of Co_3S_4 and Co_3S_4@PANI composite after the 1st and the 100th cycles are calculated using eqn (1) and (2). The D_{Na} of Co_3S_4@PANI composite after the 1st cycle is 7.15 × 10^{-15}, which is higher than that of bare Co_3S_4 (5.52 × 10^{-15}). After taking 100 cycles, although the D_{Na} of Co_3S_4@PANI composite (4.98 × 10^{-15}) experiences a slight decrease compared with the first cycle, it is three times than that of bare Co_3S_4 (1.63 × 10^{-15}). These results demonstrate that Co_3S_4@PANI composite has stable structure, fast Na^+ diffusion rate and lower polarization.

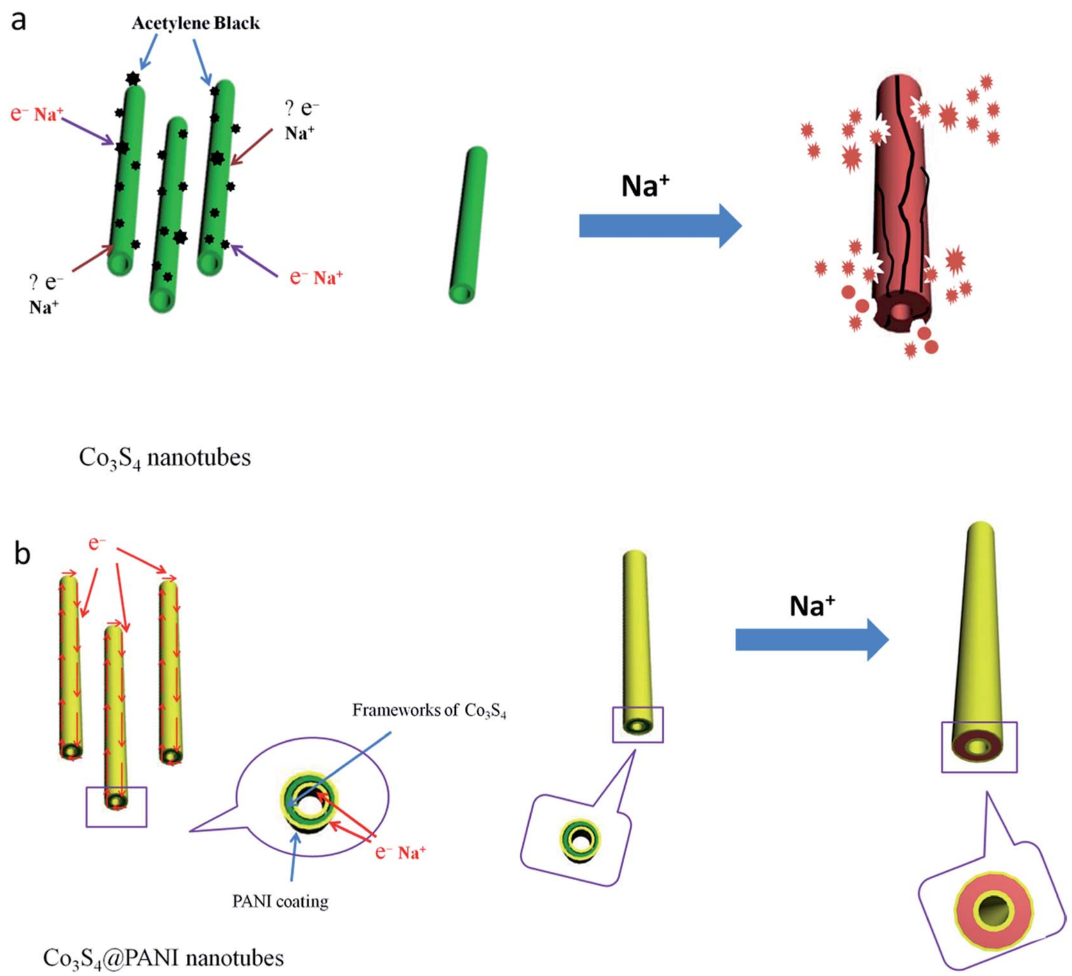

Fig. 9 Schematic electron-transfer pathways and sodium ion insertion processes for (a) bare Co_3S_4 nanotubes and (b) Co_3S_4@PANI nanotubes.

The strategy of this study can be reiterated by Fig. 9, wherein PANI coating guarantees the effective ambipolar diffusion of Na^+ and e^- into and out of the Co_3S_4 nanotubes regardless of the electrical conductivity, whereas the e^- cannot reach all the positions during the process of Na^+ intercalation for the bare Co_3S_4 nanotubes. In addition, the bare Co_3S_4 nanotubes undergo huge volume changes during Na insertion and extraction, which would result in disintegration of the electrode. However, the flexible PANI layers coated on both outer and inner surfaces of Co_3S_4 nanotubes would form "protective layers", thus preventing structure collapse during cycling. Co_3S_4@PANI composite demonstrated excellent electrochemical characteristics as an anode material for NIBs compared to the bare Co_3S_4. These include large reversible capacity, excellent rate capability, and long-term cycling stability.

4. Conclusions

Co_3S_4@PANI nanotubes synthesized *via* an *in situ* oxidative polymerization method for NIB anodes demonstrated excellent sodium-ion storage properties in terms of long cycle life and superior rate capability. The improvement of cycling performance is due to the introduction of the PANI layer, which provides efficient and rapid ion and electron transport pathways for electrochemical reactions and can also build up "protective layers" to avoid structure collapse or even pulverization of the Co_3S_4 nanotubes during cycling. These results clearly indicate that the Co_3S_4@PANI composite is one of the promising anode materials for NIBs.

Acknowledgements

This study is supported financially by the National Natural Science Foundation of China (Grant No. 51202209), the Research Foundation of Education Bureau of Hunan Province (Grant No. 15B229), the Hunan Provincial Natural Science Foundation of China (Grant No. 14JJ6017), and the Program for Innovative Research Cultivation Team in University of Ministry of Education of China (1337304). L. would also like to thank the financial support from China Scholarship Council.

References

1 J. Y. Huang, L. Zhong, C. M. J. P. Sullivan, W. Xu, L. Q. Zhang, S. X. Mao, N. S. Hudak, X. H. Liu, A. Subramanian, H. Fan, L. Qi, A. Kushima and J. Li, *Science*, 2010, **330**, 1515.
2 Y. Yang, G. Zheng and Y. Cui, *Energy Environ. Sci.*, 2013, **6**, 1552.
3 B. L. Ellis, W. R. M. Makahnouk, Y. Makimura, K. Toghill and L. F. Nazar, *Nat. Mater.*, 2007, **6**, 749.
4 V. Palomares, M. C. Cabanas, E. C. Martinez, M. H. Han and T. Rojo, *Energy Environ. Sci.*, 2013, **6**, 2312.
5 Y. Wen, K. He, Y. J. Zhu, F. D. Han, Y. H. Xu, I. Matsuda, Y. Ishii, J. Cumings and C. S. Wang, *Nat. Commun.*, 2014, **5**, 4033.
6 R. C. Massé, E. Uchaker and G. Z. Cao, *Sci. China Mater.*, 2015, **58**, 715.
7 E. Uchaker, Y. Z. Zheng, S. Li, S. L. Candelaria, S. Hu and G. Z. Cao, *J. Mater. Chem. A*, 2014, **2**, 18208.
8 H. Y. Jin, J. Dong, E. Uchaker, Q. F. Zhang, X. Z. Zhou, S. E. Hou, J. Y. Li and G. Z. Cao, *J. Mater. Chem. A*, 2015, **3**, 17563.
9 Y. Lu, L. Wang, J. Cheng and J. B. Goodenough, *Chem. Commun.*, 2012, **48**, 6544.
10 P. Ge and M. Fouletier, *Solid State Ionics*, 1988, **28**, 1172.
11 D. A. Stevensa and J. R. Dahn, *J. Electrochem. Soc.*, 2000, **14**, 1271.
12 K. Tang, L. J. Fu, R. J. White, L. H. Yu, M. M. Titirici, M. Antonietti and J. Maier, *Adv. Energy Mater.*, 2012, **2**, 873.
13 W. Luo, J. Schardt, C. Bommier, B. Wang, J. Razink, J. Simonsen and X. L. Ji, *J. Mater. Chem. A*, 2013, **1**, 10662.
14 Y. Sun, L. Zhao, H. Pan, X. Lu, L. Gu, Y. S. Hu, H. Li, M. Armand, Y. Ikuhara and L. Q. Chen, *Nat. Commun.*, 2013, **4**, 1870.
15 T. F. Zhou, W. K. Pang, C. F. Zhang, J. P. Yang, Z. X. Chen, H. K. Liu and Z. P. Guo, *ACS Nano*, 2014, **8**, 8323.
16 K. Chang and W. X. Chen, *ACS Nano*, 2011, **5**, 4720.
17 W. Xun, X. L. Wei, L. W. Yang and P. K. Shen, *J. Mater. Chem. A*, 2015, **3**, 2090.
18 Q. F. Wang, R. Q. Zou, W. Xia, J. Ma, B. Qiu, A. Mahmood, R. Zhao, Y. Y. C. Yang, D. G. Xia and Q. Xiu, *Small*, 2015, **11**, 2511.
19 R. D. Apostolova, E. M. Shembel, I. Talyosef, J. Grinblat, B. Markovsky and D. Aurbach, *Russ. J. Electrochem.*, 2009, **45**, 311.
20 Y. Gu, Y. Xu and Y. Wang, *ACS Appl. Mater. Interfaces*, 2013, **5**, 801.
21 Q. H. Wang, L. F. Jiao, H. M. Du, Y. C. Si, Y. J. Wang and H. T. Yuan, *J. Mater. Chem.*, 2012, **22**, 21387.
22 Q. H. Wang, L. F. Jiao, Y. Han, H. M. Du, W. X. Peng, Q. N. Huan, D. W. Song, Y. C. Si, Y. J. Wang and H. T. Yuan, *J. Phys. Chem. C*, 2011, **115**, 8300.
23 Y. C. Du, X. S. Zhu, X. S. Zhou, L. Y. Hu, Z. H. Dai and J. C. Bao, *J. Mater. Chem. A*, 2015, **3**, 6787.
24 Q. Zhou, L. Liu, G. X. Guo, Z. C. Yan, J. L. Tan, Z. F. Huang, X. Y. Chen and X. Y. Wang, *RSC Adv.*, 2015, **5**, 71644.
25 P. Novak, K. Muller, K. S. V. Santhanam and O. Haas, *Chem. Rev.*, 1997, **97**, 207.
26 H. P. Guo, L. Liu, Q. L. Wei, H. B. Shu, X. K. Yang, Z. H. Yang, M. Zhou, J. L. Tan, Z. C. Yan and X. Y. Wang, *Electrochim. Acta*, 2013, **94**, 113.
27 L. C. Yang, S. N. Wang, J. J. Mao, J. W. Deng, Q. S. Gao, Y. Tang and O. G. Schmidt, *Adv. Mater.*, 2013, **25**, 1180.
28 J. M. Jeong, B. G. Choi, S. C. Lee, K. G. Lee, S. J. Chang, Y. K. Han, Y. B. Lee, H. U. Lee, S. Kwon, G. Lee, C. S. Lee and Y. S. Huh, *Adv. Mater.*, 2013, **25**, 6250.
29 C. Lai, H. Z. Zhang, G. R. Li and X. P. Gao, *J. Power Sources*, 2011, **196**, 4735.
30 Z. H. Wang, X. Y. Chen, M. Zhang and Y. T. Qian, *Solid State Sci.*, 2005, **7**, 13.
31 Y. Chen, L. Hu, M. Wang, Y. Min and Y. Zhang, *Colloids Surf., A*, 2009, **336**, 64.
32 A. M. Cao, J. S. Hu, H. P. Liang, W. G. Song, L. J. Wan, X. L. He, X. G. Gao and S. H. Xia, *J. Phys. Chem. B*, 2006, **110**, 15858.

33 Y. G. Wang, W. Wu, L. Cheng, P. He, C. X. Wang and Y. Y. Xia, *Adv. Mater.*, 2008, **20**, 2166.

34 Y. G. Wang, H. Q. Li and Y. Y. Xia, *Adv. Mater.*, 2006, **18**, 2619.

35 B. Qiu, X. Y. Zhao and D. G. Xia, *J. Alloys Compd.*, 2013, **579**, 372.

36 S. G. Kang, K. M. Kim, N. G. Park, K. S. Ryu and S. H. Chang, *J. Power Sources*, 2007, **133**, 263.

37 E. O. Kirkendall, *Trans. Electrochem. Soc.*, 1942, **147**, 104.

38 J. Pu, Z. H. Wang, K. L. Wu, N. Yu and E. H. Sheng, *Phys. Chem. Chem. Phys.*, 2014, **16**, 785.

39 D. R. Cummins, H. B. Russell, J. B. Jasinski, M. Menon and M. K. Sunkara, *Nano Lett.*, 2013, **13**, 2423.

40 S. F. Kong, Z. T. Jin, H. Liu and Y. Wang, *J. Phys. Chem. C*, 2014, **118**, 25355.

41 N. Mahmood, C. Z. Zhang, J. Jiang, F. Liu and Y. L. Hou, *Chem.–Eur. J.*, 2013, **19**, 5183.

42 P. Saha, M. K. Datta, O. I. Velikokhatnyi, A. Manivannan, D. Alman and P. N. Kumta, *Prog. Mater. Sci.*, 2014, **66**, 1.

43 H. L. Pan, X. Lu, X. Q. Yu, Y. S. Hu, H. Li, X. Q. Yang and L. Q. Chen, *Adv. Energy Mater.*, 2013, **3**, 1186.

44 M. Zhou, W. Li, T. T. Gu, K. L. Wang, S. J. Cheng and K. Jiang, *Chem. Commun.*, 2015, **51**, 14354.

45 J. C. Chen, Y. Q. Liu, W. J. Li, C. Wu, L. Q. Xu and H. Yang, *J. Mater. Sci.*, 2015, **50**, 5466.

46 X. X. Zhao, Z. A. Zhang, F. H. Yang, Y. Fu, Y. Q. Lai and J. Li, *RSC Adv.*, 2015, **5**, 31465.

47 S. J. Peng, X. P. Han, L. L. Li, Z. Q. Zhu, F. Y. Cheng, M. Srinivansan, S. Adams and S. Ramakrishna, *Small*, 2016, **12**, 1359.

48 H. B. Shu, X. Y. Wang, Q. Wu and B. W. Ju, *Electrochim. Acta*, 2012, **76**, 120.